The Astrophysical Journal, 774:25 (13pp), 2013 September 1 doi:10.1088/0004-637X/774/1/25

OPACITIES AND SPECTRA OF THE *r*-PROCESS EJECTA FROM NEUTRON STAR MERGERS

Daniel Kasen[1,2], N. R. Badnell[3], and Jennifer Barnes[1,2]
[1] Department of Physics and Astronomy, University of California, Berkeley, CA 94720, USA
[2] Nuclear Science Division, Lawrence Berkeley National Laboratory, 1 Cyclotron Road, Berkeley, CA 94720, USA
[3] Department of Physics, University of Strathclyde, Glasgow G4 0NG, UK
Received 2013 March 5; accepted 2013 June 24; published 2013 August 12

ABSTRACT

Material ejected during (or immediately following) the merger of two neutron stars may assemble into heavy elements through the *r*-process. The subsequent radioactive decay of the nuclei can power transient electromagnetic emission similar to, but significantly dimmer than, an ordinary supernova. Identifying such events is an important goal of future optical surveys, offering new perspectives on the origin of *r*-process nuclei and the astrophysical sources of gravitational waves. Predictions of the transient light curves and spectra, however, have suffered from the uncertain optical properties of heavy ions. Here we argue that the opacity of an expanding *r*-process material is dominated by bound–bound transitions from those ions with the most complex valence electron structure, namely the lanthanides. For a few representative ions, we run atomic structure models to calculate the radiative transition rates for tens of millions of lines. The resulting *r*-process opacities are orders of magnitude larger than that of ordinary (e.g., iron-rich) supernova ejecta. Radiative transport calculations using these new opacities suggest that the light curves should be longer, dimmer, and redder than previously thought. The spectra appear to be pseudo-blackbody, with broad absorption features, and peak in the infrared ($\sim$1 μm). We discuss uncertainties in the opacities and attempt to quantify their impact on the spectral predictions. The results have important implications for observational strategies to find and study the radioactively powered electromagnetic counterparts to neutron star mergers.

Key words: gravitational waves – nuclear reactions, nucleosynthesis, abundances – opacity – radiative transfer – stars: neutron – supernovae: general

Online-only material: color figures

1. INTRODUCTION

Hydrodynamical simulations suggest that a small fraction of mass is ejected when two neutron stars (or a black hole and neutron star) collide or merge (Janka et al. 1999; Rosswog et al. 1999; Lee 2001; Rosswog 2005; Oechslin et al. 2007; Chawla et al. 2010; Shibata & Taniguchi 2011; Hotokezaka et al. 2013). If this ejecta is sufficiently neutron-rich, it will assemble within seconds into heavy elements via rapid neutron captures (the *r*-process; Lattimer & Schramm 1974; Eichler et al. 1989; Freiburghaus et al. 1999). The subsequent beta decay of the nuclei will heat the ejecta for days, powering a thermal, supernova-like transient (Li & Paczyński 1998). Because the ejected mass is small in comparison to ordinary supernovae (SNe), the light curves of these "*r*-process SNe" are expected to be relatively dim and short-lived. Previous radiative models predict peak bolometric luminosities around 10^{40}–10^{42} erg s^{-1}, peaking at optical wavelengths and lasting around a day (Li & Paczyński 1998; Kulkarni 2005; Metzger et al. 2010; Roberts et al. 2011; Goriely et al. 2011; Piran et al. 2013).

Although we have not yet discovered an *r*-process SN from a neutron star merger (NSM), there are compelling reasons to look for them. Because these outflows are non-relativistic, they emit radiation relatively isotropically, and are therefore promising electromagnetic counterparts to gravitational wave sources; if discovered coincidently, they could enhance the scientific value of an advanced LIGO/VIRGO gravitational wave signal (Schutz 1986; Kochanek & Piran 1993; Sylvestre 2003; Phinney 2009; Mandel & O'Shaughnessy 2010; Metzger & Berger 2012; Kelley et al. 2013; Nissanke et al. 2013). Discovery of *r*-process SNe would also dramatically illuminate our incomplete understanding of heavy element production in the universe. The NSM ejecta is thought to be a remarkably pure sample of *r*-process material, which would allow us to cleanly study heavy elements near their production site, and soon after they had been created. In principle, analysis of the light curves and spectra of these radioactive transients could be used to quantify the mass and chemical composition of the ejecta, which would clarify the unknown site(s) of *r*-process nucleosynthesis (e.g., Arnould et al. 2007; Sneden et al. 2008).

Perhaps the largest remaining uncertainty in our understanding of *r*-process SNe has concerned the opacity of the ejected debris, which (along with the ejecta mass and kinetic energy) is a key parameter determining the brightness, duration, and color of the transient. The ejecta of NSMs consists of heavy elements in rapid differential expansion, and at relatively low densities and temperatures ($\rho \sim 10^{-13}$ g cm^{-3} and $T \sim 5000$ K at 1 day after ejection). Because almost nothing is known about the optical properties of such material, previous radiative transfer models have simply adopted opacities characteristic of ordinary SNe. In Type Ia supernovae (SNe Ia), for example, the opacity is primarily due to numerous iron group lines, which are blended by Doppler broadening into a pseudo-continuum. We can expect that lines will also dominate the opacity of NSM ejecta, but unfortunately very little atomic data exists for ions heavier than the iron group, either from theory or experiment.

Given this ignorance, we might first consider some general expectations from atomic physics. The number of strong lines will be larger for ions with greater complexity—i.e., with a denser packing of low-lying energy states. Naively, one might expect higher Z elements to be more complex than the iron group. Of course, what matters is not the total number of electrons, but the number of distinct ways of distributing valence electrons within the open shells. A subshell with orbital angular

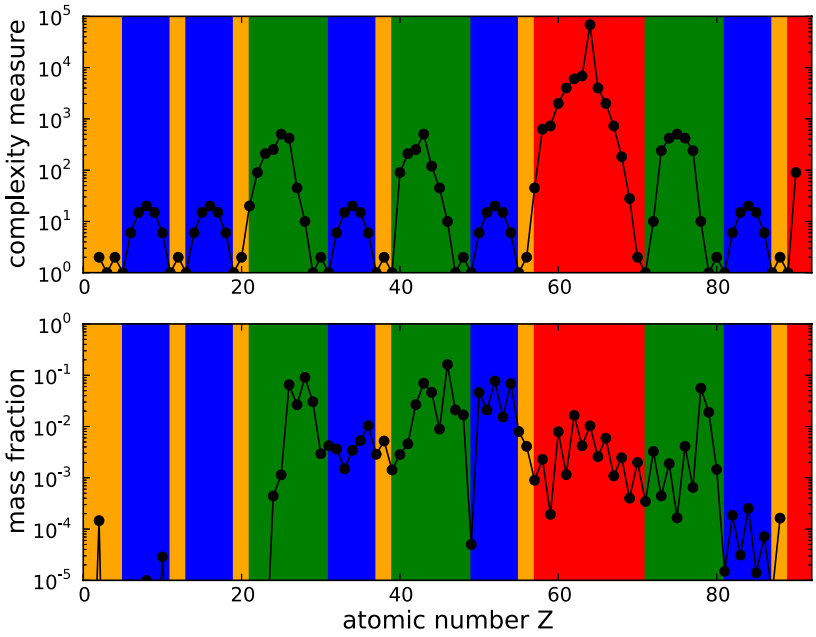

Figure 1. Complexity of the elements (top panel) and their mass fractions in the *r*-process ejecta of neutron star mergers (bottom panel). The top panel plots the number of states in the ground configuration for singly ionized ions, as estimated using the simple permutation counting of Equation (1). The pattern of peaks reflects the filling of valance shells, with the color shading giving the orbital angular momentum l (yellow = *s*, blue = *p*, green = *d*, red = *f*). The bottom panel plots the mass fractions determined in Roberts et al. (2011) by post-processing the hydrodynamical simulation of tidal tail ejecta.

(A color version of this figure is available in the online journal.)

momentum l has $g = 2(2l + 1)$ magnetic sublevels; one can estimate the number of states in a given electron configuration by simply counting the permutations of the valence electrons

$$C = \Pi_i \frac{g_i!}{n_i!(g_i - n_i)!}, \quad (1)$$

where n_i is the number of electrons in the nl-orbital labeled i, and the product runs over all open shells in a given configuration. The different terms and levels (i.e., distinct combinations of L, S, J) derived from these various permutations are split by electrostatic and fine-structure (e.g., spin-orbit) interactions. Equation (1) can thus be used to estimate the relative number of distinct energy levels of an ion, while the number of lines (i.e., radiative transitions between levels) will scale roughly as C^2. Figure 1 plots the complexity measure C for the ground configurations of singly ionized ions, where the pattern of l shell filling is clearly seen.

Equation (1) provides immediate insight into the opacity of *r*-process ejecta. Ions with valence shells of higher l are more complex, as are those whose open shells are closer to half filled. This is why the iron group, with a nearly half-filled d ($l = 2$) shell, usually dominates the line opacity in typical astrophysical mixtures. Heavy *r*-process ejecta, however, includes uncommon species of even greater complexity. Of particular importance are the lanthanides ($58 < Z < 70$) and the actinides ($90 < Z < 100$) which, due to the presence of an open f ($l = 3$) shell, have complexity measures roughly an order of magnitude greater than the iron group. While the actinide series is generally of very low abundance, the lanthanides may represent several percent of *r*-process material by mass. We will find that these species dominate the total opacity of NSM ejecta, resulting in opacities ~10–100 times greater than previously assumed.

To calculate the ejecta opacity in detail, we need a comprehensive list of atomic lines. As almost no data is available for heavy ions, we turn here to ab initio atomic structure modeling using the `Autostructure` code (Badnell 2011). These models determine the approximate ion energy level structure and the wavelengths and oscillator strengths of all permitted radiative dipole transitions (Section 3). Without fine tuning the structure model, the computed energies and line wavelengths are not exact. Fortunately, the effective opacity in an expanding medium is a wavelength average over many lines. Because our models reasonably capture the statistical distribution of levels and lines, they can be used to derive fairly robust estimates of the pseudo-continuum opacity (Sections 4 and 5).

Modeling the radiative properties of all high Z ions is a long term endeavor; here we present initial structure calculations for a few representative ions selected from the iron group (Fe, Co, Ni), the lanthanides (Ce, Nd), and a few other heavy *d*-shell and *p*-shell ions (Os, Sn). The `Autostructure` line data is then used to calculate the opacity of expanding ejecta under the assumption of local thermodynamic equilibrium (LTE). We show that ions of similar complexity have similar properties, which allows us to estimate the total opacity of an *r*-process mixture based on the representative species (Section 6).

The derived opacities can be input into a multi-wavelength, time-dependent radiative transfer code to predict the observable properties of *r*-process SNe (Section 7). We discuss here the general spectroscopic properties of these transients, while a companion study explores the broadband light curves and their dependence on the ejecta properties (Barnes & Kasen 2013). In general, the high *r*-process opacities result in light curves that are significantly broader, dimmer, and redder than the previously believed. These results have important implications for observational strategies to find and interpret the radioactively powered electromagnetic counterparts to NSMs.

2. OPACITY OF RAPIDLY EXPANDING EJECTA

We set the stage by reviewing the physical properties of the material expected to be ejected in NSMs. We then describe the

nature of the opacity in such gas, in particular that arising from line interactions in a rapidly expanding medium.

2.1. Physical Conditions of the Ejecta

There are at least two distinct mechanisms by which material may be ejected in NSMs: (1) during the merger, surface layers may be tidally stripped and dynamically flung out in "tidal tails." (2) Following the merger, material which has accumulated in a centrifugally supported disk may be blown off in a neutrino- or nuclear-driven wind (Levinson 2006; Surman et al. 2006; Metzger et al. 2008, 2009). The amount of mass ejected in the tidal tails appears to depends upon many factors: the NS mass ratio, the equation of state of nuclear matter, and the treatment of gravity, but simulations give values in the range $M_{\rm ej} = 10^{-4}$–$10^{-1}\ M_\odot$. A similar amount of mass may potentially be ejected in the disk wind. In both cases, the characteristic velocities are $v_{\rm ej} \approx 0.1$–$0.3c$, of the order of the escape velocity from a NS.

The composition of the material ejected by the two mechanisms is likely different. The tidal tail ejecta is initially cold and very neutron-rich (electron fraction $Y_e \sim 0.1$), and should rapidly assemble into heavy elements ($Z > 50$) through the *r*-process. The conditions in the disk wind are quite different; weak interactions will drive the material to be less neutron-rich ($Y_e \approx 0.5$) and the entropy will be higher. This environment is more similar to the neutrino-driven wind from proto-neutron stars in core collapse SNe. It is unclear whether a robust *r*-process occurs in such a wind, or whether the distribution only extends to atomic numbers $Z \sim 50$. If neutrinos drive Y_e close to 0.5, the composition may be dominated by radioactive ^{56}Ni (Surman et al. 2008).

Soon after the mass ejection (∼100s of seconds), hydrodynamical and nucleosynthetic processes abate and the ejecta reaches a phase of free expansion. In the absence of any forces, the velocity structure becomes homologous—i.e., the velocity of any mass element is proportional to radius, $v = rt_{\rm ej}$, where $t_{\rm ej}$ is the time since homology sent in. The density of the ejecta at 1 day can be estimated

$$\rho_0 \approx \frac{M_{\rm ej}}{(4\pi/3)v_{\rm ej}^3 t_{\rm ej}^3} \approx 2.8\times10^{-13}\,\frac{M_{-2}}{v_{0.1}^3 t_d^3}\ {\rm g\ cm^{-3}}, \qquad (2)$$

where $M_{-2} = M_{\rm ej}/10^{-2}\ M_\odot$, $v_{0.1} = v_{\rm ej}/0.1c$, and $t_d = t_{\rm ej}/{\rm day}$. In just a day, the density of the ejecta has dropped by ∼20 orders magnitude from its original value in the neutron star.

The ejecta material initially cools very effectively by expansion, but will be reheated by the decay of *r*-process nuclei. Radioactive energy is released in the form of gamma-rays, beta particles, and fission fragments, which will be thermalized, to various degrees, by scattering within the ejecta (Metzger et al. 2010). The heated material will radiate, and thermal photons will escape the medium on the effective diffusion timescale for a homologously expanding medium (Arnett 1980)

$$t_{\rm d} \sim \left[\frac{M_{\rm ej}\kappa}{v_{\rm ej}c}\right]^{1/2} \sim 1.7 M_{-2}^{1/2} v_{0.1}^{-1/2}\kappa_{0.1}^{1/2}\ {\rm days}, \qquad (3)$$

where the opacity κ of the ejecta has been normalized to a value $\kappa_{0.1} = \kappa/0.1\ {\rm cm^2\ g^{-1}}$, a value appropriate for iron group elements (but not, we will find, for *r*-process elements). This timescale for diffusion sets the duration of the radioactively powered light curve.

The luminosity near the peak of the light curve will be of the order of the instantaneous rate of energy deposition $L \approx M_{\rm ej}\dot\epsilon$, where $\dot\epsilon$ is the radioactive energy released per unit time per unit gram (Arnett 1982). Stefan's law, $L = 4\pi r^2\sigma_{\rm sb}T^4$, provides an estimate of the surface temperature

$$T \approx \left[\frac{M_{\rm ej}\dot\epsilon}{\sigma v_{\rm ej}^2 t_{\rm ej}^2}\right]^{1/4} \approx 10^4 M_{-2}^{1/4}(v_{0.1}t_d)^{-1/2}\ {\rm K}. \qquad (4)$$

For times $t_{\rm ej} \gtrsim 1$ day, the characteristic temperatures and densities of NSM ejecta are thus roughly in the range $T \sim 10^3$–10^4 K and $\rho \sim 10^{-16}$–10^{-12} g cm^{-3}. Under these conditions, and assuming LTE, the gas will be in a low ionization state, being mostly singly or doubly ionized near the photosphere.

2.2. Local Thermodynamic Equilibrium

We adopt LTE to compute level populations in this paper, a necessary approximation given the complexity of the ions involved. The low density of NSM ejecta at $t_{\rm ej} \gtrsim 1$ day is not sufficient for collisional processes alone to establish LTE. However, in the optically thick regions below the photosphere, the radiation field will tend toward a blackbody distribution and radiative transitions will drive the level populations to their LTE values. Because the effective diffusion time and spectral energy distribution (SED) are mostly set by processes near and below the photosphere, LTE calculations likely provide a reasonable first approximation. At late times ($t \gtrsim 20$ days), when the entire remnant becomes transparent, LTE will break down at all radii and result in poor SED predictions.

Considering the heavily radioactive environment of NSM ejecta, one may worry that, even at early times, departures from LTE may be driven by non-thermal ionization/excitation processes (namely, impacts by fast electrons that have been Compton scattered by radioactive gamma-rays). As a rough estimate of the potential effects, we compare the rates for a bound–bound transition of energy ΔE. The non-thermal excitation rate is $R_{\rm nt} \approx f\dot\epsilon/\Delta E$, where $\dot\epsilon$ is the radioactive power released per particle, and f is the fraction of that power that goes into excitation (as opposed to ionization or thermalization). The radiative excitation rate, assuming a blackbody field, is $R_{\rm bb} = B_{12}B_\nu(T)$ where B_{12} is the Einstein absorption coefficient and $B_\nu(T)$ the Planck function. Using the Einstein relations, the ratio of rates is

$$\frac{R_{\rm nt}}{R_{\rm bb}} \approx \left[\frac{f\dot\epsilon}{\Delta E A_{21}}\right](e^{\Delta E/kT} - 1), \qquad (5)$$

where the Einstein spontaneous emission coefficient $A_{21} \sim 10^8$–10^9 for permitted optical transitions. For *r*-process ejecta at 1 day, Metzger et al. (2010) find $\dot\epsilon \approx 1\ {\rm eV\ s^{-1}}$ Considering values $\Delta E \sim 1$ eV, $T \approx 5000$ K and $f \sim 1/3$, the ratio $R_{\rm nt}/R_{\rm bb} \approx 10^{-8}$. Non-thermal transitions are therefore negligible except for transitions well above the thermal energy ($\Delta E/kT \gtrsim 20$). A similar argument can be made for non-thermal ionization. We conclude that the radioactive energy deposition will likely not seriously undermine our LTE assumption, except at late times when the ejecta becomes rather cold and transparent.

2.3. Line Expansion Opacity

The opacity of bound–bound transitions is significantly enhanced by the high expansion velocities found in SN and NSM

ejecta (Karp et al. 1977). We discuss here the "expansion opacity" formalism which wavelength averages the contribution of multiple lines and treats the line radiative transfer in the Sobolev approximation.

As a photon propagates through the differentially expanding medium, its wavelength is constantly Doppler shifted with respect to the comoving frame. For a homologous (Hubble-like) expansion, this Doppler shift is always to the red, and proportional to the distance traveled. The photon will interact with a line when its comoving frame wavelength is redshifted into resonance with the line rest wavelength. The spatial extant of this interaction, or resonance, region is set by the intrinsic width of the line profile. If, for example, the line width is due to the thermal velocity, Δv_t, of ions, the physical size of the resonance region is $\Delta s \sim \Delta v_t t_{\rm ej}$.

Because the thermal velocities in NSM ejecta are very small ($v_t \sim 1$ km s^{-1}) compared to the ejecta velocities ($v_{\rm ej} \approx 10^5$ km s^{-1}), the resonance region of a line is tiny compared to the ejecta scale height, and the matter properties can be taken to be constant over the region. This is the essence of the Sobolev approximation (Sobolev 1960). In this limit, the line extinction coefficient can be analytically integrated to give the Sobolev optical depth across the resonance region

$$\tau_s = \frac{\pi e^2}{m_e c} f_{\rm osc} n_{\rm l} t_{\rm ej} \lambda_0, \tag{6}$$

where $f_{\rm osc}$ is the oscillator strength and λ_0 the rest wavelength of the line. The Sobolev optical depth is a local quantity which depends on $n_{\rm l}$, the number density in the lower level of the transition at the location of resonance. The probability that a photon interacts (i.e., is scattered or absorbed) a least once in traversing the resonance region is simply $1 - e^{-\tau_s}$.

A photon traveling through the expanding medium comes into resonance with lines one-by-one, sweeping from blue to red. The effective mean free path depends not on the strength of any one line, but rather on the wavelength spacing of strong ($\tau_s \gg 1$) lines, which can be quantified as follows. Say that within some wavelength region $(\lambda_i, \lambda_i + \Delta\lambda_i)$ we have N strong lines. The spacing between the lines is, on average, $\Delta\lambda_i/N$ and the velocity gradient which Doppler shifts a photon from one line to the next is $\Delta v_s/c = \Delta\lambda_i/\lambda_i N$. If homologous expansion holds, the distance a photon travels between line interactions is then $l_{\rm mfp} = \Delta v_s t_{\rm ej}$. This is an estimate of the mean-free path, while the inverse quantity, $l_{\rm mfp}^{-1}$, defines the matter extinction coefficient (units cm^{-1})

$$\alpha_{\rm ex} \approx \frac{1}{l_{\rm mfp}} \approx \frac{N}{\Delta\lambda_i}\frac{\lambda_i}{c t_{\rm ej}}, \tag{7}$$

where the bin size $\Delta\lambda_i$ can be chosen arbitrarily to average over a reasonable number of lines.

A formal derivation along these lines was introduced by Karp et al. (1977) to estimate the extinction coefficient in an expanding medium. We use here the slightly modified expression developed by Eastman & Pinto (1993)

$$\alpha_{\rm ex}(\lambda) = \frac{1}{c t_{\rm ej}} \sum_i \frac{\lambda_i}{\Delta\lambda_i}[1 - e^{-\tau_i}], \tag{8}$$

where the sum runs over all lines in the wavelength bin $\Delta\lambda_i$. Equation (8) takes into account the cumulative effect of many weak lines; in the case where all lines are optically thick ($\tau_s \gg 1$), it reduces to the simple estimate equation (7).

An interesting property of the expansion opacity is the dependence on ion density, which appears only in the Sobolev optical depth, τ_s. In the limit that all lines are weak, the density dependence is linear. However, in the opposite limit where all lines are very optically thick, the extinction coefficient is independent of density. In our actual calculations, the density dependence (which is set by the statistical distribution of line optical depths) is weak, roughly logarithmic. As a consequence, certain ions can make a significant contribution to the opacity even when their abundance is very low.

The expansion opacity (units cm^2 g^{-1}) of bound–bound transitions is related to $\alpha_{\rm ex}$ by

$$\kappa_{\rm ex}(\lambda) = \frac{\alpha_{\rm ex}}{\rho} = \frac{1}{c t_{\rm ej}\rho} \sum_i \frac{\lambda_i}{\Delta\lambda}[1 - e^{-\tau_i}]. \tag{9}$$

Given the weak dependence of $\alpha_{\rm ex}$ on density, the line expansion opacity actually increases as the density drops.

2.4. Applicability of the Sobolev Approximation

At least three conditions must be met for the Sobolev approximation, which underlies the expansion opacity expression equation (9), to be valid. The first, already mentioned, is that the thermal velocity of the ions (presumed to set the intrinsic line widths) must be significantly smaller than the velocity scales over which the ejecta properties vary. For NSM ejecta, the ratio is $v_t/v_{\rm ej} \approx 10^{-5} \ll 1$, which assures the applicability of the narrow line limit.

A second condition, relevant for time-varying environments, is that the time photons spend within a resonance region be short compared to the timescale over which the ejecta properties vary (e.g., the expansion timescale). For strong lines, a photon may scatter multiple times within the resonance region before finally being redistributed to the edge of the line profile and escaping (i.e., redshifting past) the transition. In the Sobolev formalism, the probability that a photon escapes the line after a scatter is

$$\beta = \frac{1 - e^{-\tau_s}}{\tau_s} \approx \tau_s^{-1} \text{ for } \tau \gg 1, \tag{10}$$

and the average number of scatters in a thick line is $N_{\rm sc} \sim 1/\beta$. Assuming the distance traveled between scatters is, on average, $v_{\rm t} t_{\rm ej}$, the time spent in the resonance region is $t_{\rm sc} \sim N_{\rm sc} v_{\rm t} t_{\rm ej}/c$. The condition $t_{\rm sc} < t_{\rm ej}$ sets a limit on the optical depth of the line $\tau_s \lesssim c/v_{\rm t} = 3 \times 10^5 v_{t,1}$, where $v_{t,1} = v_t/1$ km s^{-1}. In practice, optical depths $>3 \times 10^5$ are regularly encountered, in particular for resonance lines. In most cases, however, fluorescence provides an avenue for escape. The probability of deexcitation to a lower level is suppressed by a factor of β, and so it is likely that the ion will eventually deexcite via a cascade through multiple low τ_s transitions. This generally evades the problem of extended line trapping, except perhaps for those few transitions in which fluorescence is not possible.

A third condition is that the intrinsic profiles of strong lines must not, in general, overlap, as this would introduce a coupling of the radiative transport between lines. In particular, a photon that escapes from the red edge of one line will have an enhanced probability of escaping a second overlapping line. This invalidates the sum in Equation (9) which assumes an independent interaction probability for each line. Overlap of weak lines (which are extremely numerous in our calculations) is common; however, this likely does not introduce any serious error, as the τ_s dependence is linear when $\tau_s \ll 1$. Moreover,

the opacity is usually dominated by the strong lines. Occasional overlap of strong lines is inevitable, and may moderately reduce the expansion opacity at certain wavelengths. The entire Sobolev formalism, however, becomes inapplicable when the wavelength spacing of strong lines, $\Delta\lambda/N$, becomes comparable to the intrinsic (e.g., thermal) width $\Delta\lambda_t = \lambda_0(v_t/c)$ of the lines. From Equation (9), we can define an opacity when such "saturation" occurs:

$$\kappa_{\rm sat} = \frac{\lambda_0}{\Delta\lambda_t}\frac{1}{\rho c t_{\rm ej}} = \frac{1}{\rho v_t t_{10}} \approx 10^3 \rho_{-13} t_1^{-1} v_{t,1}^{-1}\ {\rm cm}^2\ {\rm g}^{-1}. \quad (11)$$

When $\kappa_{\rm ex} > \kappa_{\rm sat}$, strong line overlap is the norm and the Sobolev expansion opacity formalism can no longer be trusted to return reasonable values. Under some conditions, and at certain wavelengths, we will find that our calculated *r*-process opacities approach or exceed saturation, such that this issue may be a serious concern.

2.5. Other Sources of Opacity

Other potential sources of opacity include free–free (i.e., bremsstrahlung), bound-free (i.e., photoionization), and electron scattering. In NSM ejecta, none of these turn out to be important compared to bound–bound. For example, the wavelength independent electron scattering opacity is given by

$$\kappa_{\rm es} = \frac{\bar{x}\sigma_t}{\bar{A}m_p} \approx 0.4\left(\frac{\bar{x}}{\bar{A}}\right)\ {\rm cm}^2\ {\rm g}^{-1}, \quad (12)$$

where $\bar{x}$ is the mean ionization fraction and $\bar{A}$ the mean atomic weight of the ions. For NSM ejecta comprised of lowly ionized ($\bar{x} \sim 1$) heavy elements ($\bar{A} \sim 130$), $\kappa_{\rm es}$ is a factor $\bar{x}/\bar{A} \sim 10^{-2}$ smaller than the typical value for ionized hydrogen, and much less than the *r*-process line opacity at all wavelengths of interest.

The free–free opacity for a gas in ionization state $\bar{x} \sim 1$ is given approximately by (e.g., Rybicki & Lightman 1986)

$$\kappa_{\rm ff} = 0.005\frac{\bar{x}^3}{A^2}\rho_{-13}T_4^{-1/2}(\lambda/1\ \mu{\rm m})^3\ {\rm cm}^2\ {\rm g}^{-1}, \quad (13)$$

where we have set the correction for stimulated emission and the Gaunt factor to unity. For the low densities and $\bar{x}/\bar{A}$ values found in NSM ejecta, the free–free opacity at the relevant wavelengths is negligible ($\kappa_{\rm ff} \approx 10^{-6}$ cm^2 g^{-1}).

Finally, the opacity due to a bound-free transition for photons at the threshold energy (where the cross-section is largest) for some excited level of an ion is given by

$$\kappa_{\rm bf} = \frac{\sigma_0}{\bar{A}m_p}\frac{e^{-\Delta E/kT}}{Z(T)}, \quad (14)$$

where ΔE is the excitation energy of the level and $Z(T)$ the partition function (LTE is assumed). In order for the bound-free transition to apply to optical/infrared photons, the level must be a highly excited state, $\Delta E \gtrsim \chi - 2$ eV, where χ is the ionization potential. As a representative estimate of the opacity at $T = 5000$ K, we consider a singly ionized heavy element with $A = 120$, $\Delta E \sim 8$ eV and $Z(T) = 20$ and adopt the hydrogenic value $\sigma_0 \approx 6 \times 10^{-18}$cm^2. The resulting opacity at threshold is also very small, $\kappa_{\rm bf} \approx 1.3 \times 10^{-5}$ cm^2 g^{-1}, due mainly to the Boltzmann factor. At ultraviolet wavelengths ($\lambda \lesssim 1000$ Å), the bound-free opacity may actually dominate, since, for low lying levels, ($\Delta E \approx 0$) one finds $\kappa_{\rm bf} \approx 10^3$ cm^2 g^{-1}.

3. ATOMIC STRUCTURE CALCULATIONS

To estimate the radiative data for high-*Z* elements, we used the `Autostructure` program (Badnell 2011). This code was used previously to calculate data up to Ni for the updated opacities of the Opacity Project (Badnell et al. 2005). Recent developments (Badnell et al. 2012) have enabled it to be used to make extensive calculations of radiative (and autoionization) rates for a half-open *f*-shell. `Autostructure` calculates the approximate level energy structure of ions, and all relevant radiative transition rates, given a user-specified set of electron configurations. The many-electron quantum mechanical problem is treated using a multi-configuration wavefunction expansion with a Breit-Pauli Hamiltonian. We used the kappa-averaged relativistic wavefunction option as introduced by Cowan & Griffin (1976). The radial orbitals were determined using a Thomas–Fermi–Dirac–Amaldi potential. As the standard *LS*-coupling scheme breaks down for high *Z* elements, we adopted a level-resolved intermediate coupling scheme.

We used the NIST (Kramida et al. 2012) atomic database to identify the electron configurations corresponding to the ground and low-lying states of each ion. For several of the high-*Z* ions, the NIST data appeared to be incomplete, and we included additional configurations suspected to be relevant. Table 1 lists the configurations used for each ion. For the lanthanides, the highest *nl* orbital we considered was the 6*p* one. We experimented with including configurations generated by electron promotion to higher orbitals (e.g., $n = 7, 8$), however, these typically produced highly excited levels not significantly thermally populated under the relevant physical conditions. As we did not note any large effects on the opacities, we omit these configurations from our final calculations, although more exhaustive explorations of configuration space are certainly warranted.

`Autostructure` includes a dimensionless radial scaling parameter for each *nl*-orbital, which must be optimized to establish a realistic level structure for low-charge ions. The optimization consists of varying the scaling parameters so as to minimize a user-specified weighted sum of eigenenergies. The closed-shell core cannot be excluded from the structural optimization of complex heavy near-neutral ions because of the strength of core polarization effects on the valence orbitals (Palmeri et al. 2000). We therefore used a single common variational scaling parameter for all closed-shell orbitals, but varied the parameters of the valence orbitals independently. This ab initio optimization procedure does not require any observed energies. Thus, it is ideally suited to situations such as the present one where the observed data is at best sparse.

We explored several strategies for optimization. The first—which we label *opt1*—was to simultaneously vary the scaling parameters for all included (core-plus-valence) orbitals and to minimize the equally weighted sum of all energy levels included by the configuration expansion. This has the advantage of not biasing the structure toward any given configuration(s), which is valuable given that we seek radiative data for many excited levels. The disadvantage is that it gives no due preference to the ground state, and thus does not always predict a ground state configuration in agreement with what is deduced experimentally. Figure 2 shows the energy level structure for Nd II, where it is seen that the *opt1* optimization predicts the wrong ground configuration. While for many applications this would be a fatal flaw, in the present context we expect several low lying configurations to be significantly populated, in which

Table 1
Autostructure Atomic Structure Models

Ion	Configurations Included[a]	Levels	Lines	χ[b] (eV)
Fe I	$\mathbf{3d^64s^2}$, $3d^74s$, $3d^64s4p$, $3d^74p$, $3d^74d$, $3d^74f$, $3d^75s$, $3d^75p$, $3d^75d$, $3d^64s4d$	1784	326, 519	7.90
Fe II	$\mathbf{3d^64s}$, $3d^7$, $3d^64p$, $3d^64d$, $3d^64f$, $3d^65s$, $3d^65p$, $3d^65d$, $3d^54s^2$, $3d^54s4p$	1857	355, 367	16.18
Fe III	$\mathbf{3d^6}$, $3d^54s$, $3d^54p$, $3d^54d$, $3d^54f$, $3d^55s$, $3d^55p$, $3d^55d$, $3d^44s4p$	2050	420, 821	30.65
Fe IV	$\mathbf{3d^5}$, $3d^44s$, $3d^44p$, $3d^44d$, $3d^44f$, $3d^45s$, $3d^45p$, $3d^45d$	1421	217, 986	54.91
Co I	$\mathbf{3d^74s^2}$, $3d^84s$, $3d^74s4p$, $3d^9$, $3d^84p$, $3d^84d$, $3d^85s$, $3d^74s4d$, $3d^74s5s$	778	62, 587	7.88
Co II	$\mathbf{3d^8}$, $3d^74s$, $3d^64s^2$, $3d^74p$, $3d^64s4p$, $3d^75s$, $3d^74d$	757	58, 521	17.08
Co III	$\mathbf{3d^7}$, $3d^64s$, $3d^64p$, $3d^64d$, $3d^65s$	601	34, 508	33.50
Co IV	$\mathbf{3d^6}$, $3d^54s$, $3d^54p$, $3d^54d$, $3d^55s$	728	48, 254	51.27
Ni I	$\mathbf{3d^84s^2}$, $3d^{10}$, $3d^84s4p$, $3d^94s$, $3d^94p$, $3d^94d$, $3d^94f$, $3d^95s$, $3d^95p$, $3d^96s$	174	2, 776	7.64
Ni II	$\mathbf{3d^9}$, $3d^84s$, $3d^84p$, $3d^84d$, $3d^84f$, $3d^85s$, $3d^85p$, $3d^86s$, $3d^74s4p$, $3d^74s^2$	520	25, 496	16.18
Ni III	$\mathbf{3d^8}$, $3d^74s$, $3d^74p$, $3d^74d$, $3d^74f$, $3d^75s$, $3d^75p$, $3d^76s$, $3d^64s^2$	1644	61, 108	35.19
Ni IV	$\mathbf{3d^7}$, $3d^64s$, $3d^64p$, $3d^64d$, $3d^64f$, $3d^65s$, $3d^65p$, $3d^66s$, $3d^54s4p$, $3d^54s^2$	751	258, 305	54.92
Nd I	$\mathbf{4f^46s^2}$, $4f^35d6s^2$, $4f^45d6s$, $4f^45d^2$, $4f^35d6s6p$, $4f^45d6p$	18104	24, 632, 513	5.52
Nd II	$\mathbf{4f^46s}$, $4f^45d$, $4f^46p$, $4f^35d^2$, $4f^35d6s$, $4f^35d6p$, $4f^36s6p$	6888	3, 873, 372	10.7
Nd III	$\mathbf{4f^4}$, $4f^35d$, $4f^36s$, $4f^36p$, $4f^25d^2$, $4f^25d6s$, $4f5d^26s$	1650	232, 715	22.14
Nd IV	$\mathbf{4f^3}$, $4f^25d$, $4f^26s$, $4f^26p$	241	5780	40.4
Ce II	$\mathbf{4f5d^2}$, $4f5d6s$, $4f^26s$, $4f^25d$, $4f6s^2$, $4f5d6p$, $4f^26p$, $5d^3$, $4f6s6p$, $4f^3$	5, 637	4, 349, 351	10.8
Ce III	$\mathbf{4f5d}$, $4f6s$, $5d^2$, $4f6p$, $5d6s$	3, 069	868, 640	20.19
Os II	$\mathbf{5d^66s}$, $5d^65f$, $5d^65g$, $5d^66s$, $5d^66p$, $5d^66d$, $5d^66f$, $5d^66g$	3271	1, 033, 972	17.0
Sn II	$\mathbf{5s^25p}$, $5s^24f$, $5s^25d$, $5s^26s$, $5s^26p$, $5s5p^2$, $5s5p6s$, $5s5p6p$	47	371	14.63

Notes.
[a] Electron configurations used in the auto structure calculations. Ground states (from NIST) are in bold.
[b] Ionization potential, taken from NIST.

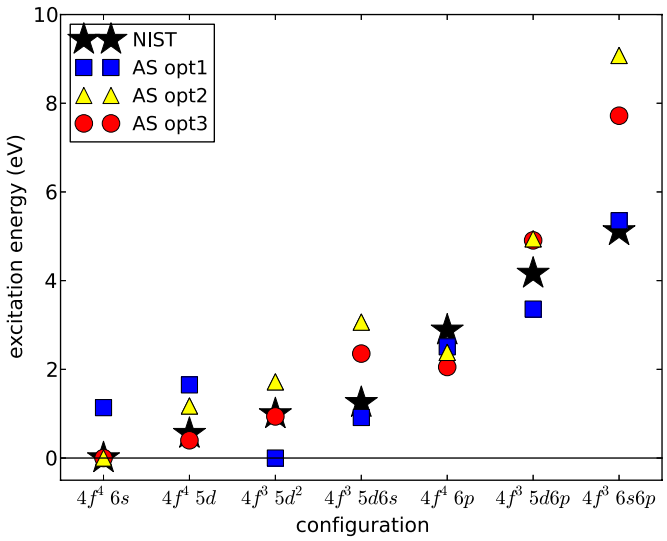

Figure 2. Atomic structure model calculations of the excitation energy of the lowest level of Nd II electron configurations. The circles denote the results from `Autostructure` obtained under various optimization approaches (described in the text). The stars denote the experimental energies from NIST.
(A color version of this figure is available in the online journal.)

case the mean line opacity may be less sensitive to the exact configuration ordering.

We considered a second strategy (*opt2*) whereby the above optimization was first applied to only those orbitals included in the ground configuration. These scaling parameters were then fixed, and a second optimization was carried out varying the parameters of all remaining orbitals. This method usually produced the correct ground state configuration. The energies of the excited levels were also close to but a bit higher than the available NIST values, and overall not as good as those found using the *opt1* approach (Figure 2).

The model structure can be further refined by iteratively adjusting the scaling parameters by hand. We attempted this for Nd II, guided by the trends found in the *opt1* and *opt2* calculations. An improved solution was found (*opt3*) which reproduced the ground and first two excited level energies almost exactly. Further iterations could presumably improve the result, but this sort of manual alignment is time consuming, and more of an art than science. We attempted this *opt3* approach only for Nd II, which is the most important ion for our *r*-process light curve calculations.

4. IRON GROUP OPACITIES

4.1. Comparison to Kurucz Line Data

The atomic properties of $Z < 30$ ions are reasonably well known based on experiment and previous structure modeling. In particular, R. Kurucz has generated extensive line lists, including CD23 (∼500,000; Kurucz & Bell 1995a) and CD1 (∼42 million lines; Kurucz 1993). These lists (which are dominated by iron group lines) have been derived from atomic structure calculations using the Cowan code (Cowan 1981) which have been iteratively tuned to reproduce the extensive observed experimental level energies (Kurucz & Bell 1995b). SN modelers have used the Kurucz data to successfully model the optical light curves and spectra of observed (iron-rich) SNe Ia (e.g., Kasen et al. 2009; Sim et al. 2010) which suggests that, for the iron group, the Kurucz line data can be taken to be reasonably accurate and complete.

To validate our ab initio `Autostructure` line data against the observationally constrained data of Kurucz, we ran structure models for the first four ionization stages of Fe, Co, and Ni, using the electron configurations listed in Table 1. Unlike Kurucz, we made no attempt (beyond our ab initio *opt1* optimization scheme) to tune the model, and our calculated level energies can differ from the experimental values by factors of two or more.

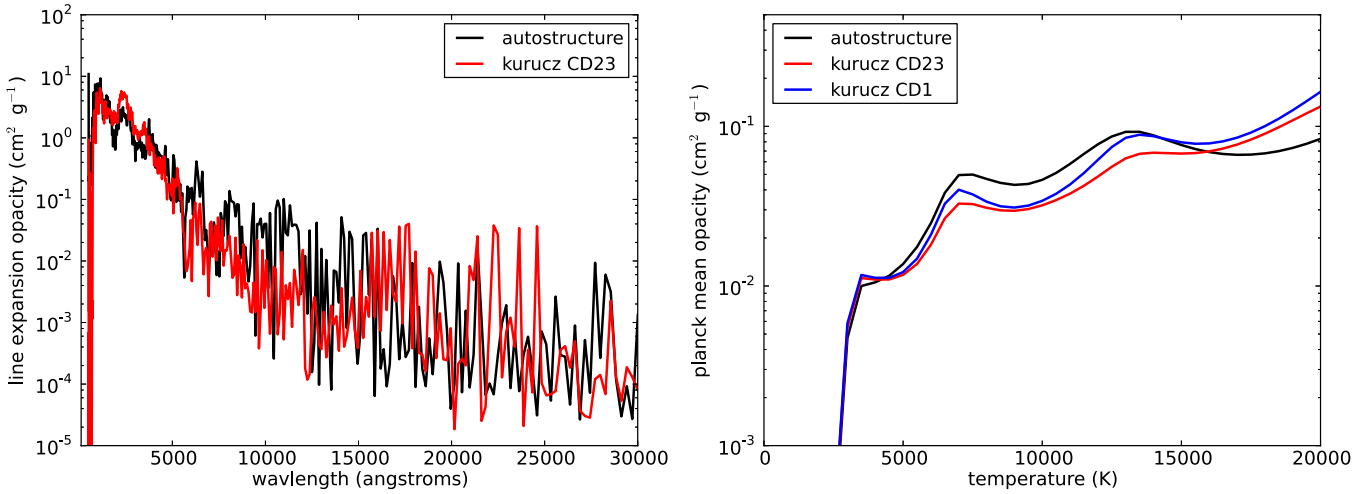

Figure 3. Calculated line expansion opacities for a mixture of iron group elements (10% Ni, 80% Co, 10% Fe) representative of decayed ^{56}Ni. The right panel plots the Planck mean opacity vs. temperature, while the left panel plots the wavelength dependence of the opacity at a specific temperature, $T = 5000$ K. The opacities calculated using our `Autostructure`-derived line data generally agree with those using the Kurucz linelists. The calculations assume $\rho = 10^{-13}$ g cm^{-3}, $t_{\rm ej} = 10$ days, and a wavelength binning $\Delta\lambda = 0.01\lambda$.

(A color version of this figure is available in the online journal.)

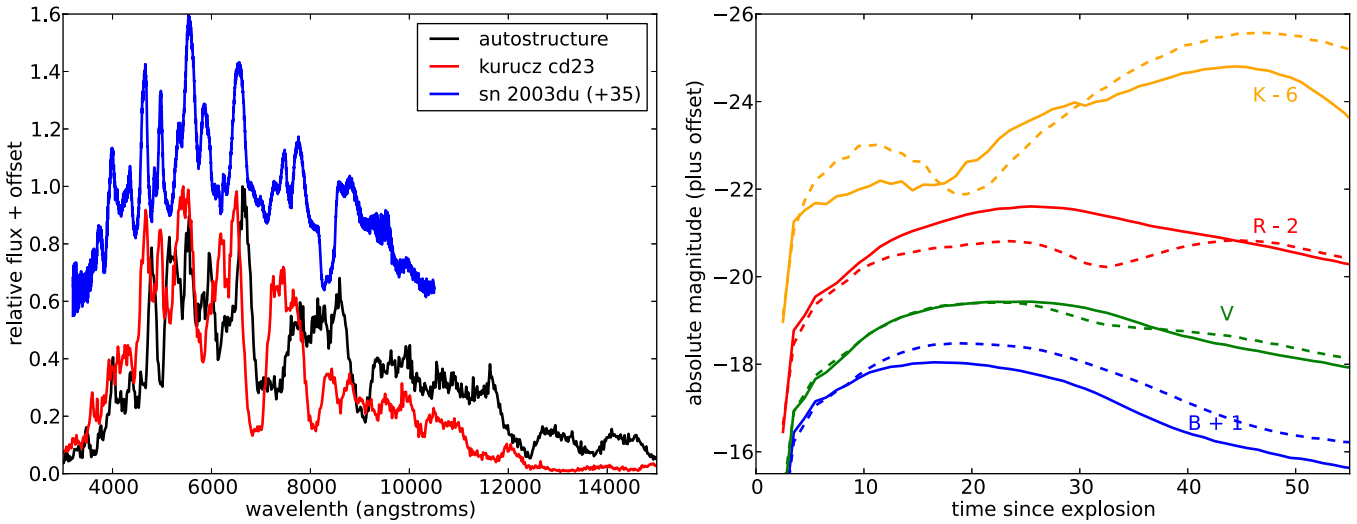

Figure 4. Synthetic light curves and spectra of a model consisting of pure ^{56}Ni ejecta, computed with different line data. The left panel shows that the SED (at 50 days after merger) calculated using the `Autostructure` line data resembles that obtained using the Kurucz data. Both resemble the spectrum of the Type Ia SN 2003du observed 34 days after peak (∼52 days after explosion). The right panel compares the broadband light curves of the model calculated using the `Autostructure` line data (solid lines) and the Kurucz CD23 linelist (dashed lines).

(A color version of this figure is available in the online journal.)

Nevertheless, we find that our derived iron group expansion opacities are in good agreement with those of Kurucz (Figure 3). Our Planck mean opacities differ from those of Kurucz by only ∼30% over the temperature range 1000–20,000 K, and the wavelength dependence of the opacity is quantitatively similar, with the opacity rising sharply to the blue. The good agreement indicates that our `Autostructure` calculations capture the statistical properties of the lines, even if the individual energy levels and line wavelengths may be inaccurate.

4.2. Application to Supernova Modeling

To demonstrate how our `Autostructure` derived iron group opacities perform in a real transport calculation, we calculated synthetic light curves and spectra of a simple SN Ia model. As a numerical "thought" experiment, we pretended that our understanding of SNe Ia was as rudimentary as it is for NSM outflows, and that our only expectation was that a carbon/oxygen star was burned to nuclear statistical equilibrium (NSE). We thus constructed a spherically symmetric ejecta model consisting of uniform density, initially pure ^{56}Ni with a total mass of 1 $M_\odot$ and kinetic energy of 10^{51} erg, roughly the nuclear energy released in burning the C/O to NSE. Of course, real SN Ia are not homogenous, and, in addition to ^{56}Ni, are observed to contain a significant amount of intermediate mass elements (IMEs, Si, S, Ca).

We calculated synthetic observables of this ejecta model using the time-dependent, multi-wavelength radiation transport code `Sedona` (Kasen et al. 2006), and assuming that the level populations were in LTE. Figure 4 shows that, despite the simplistic nature of the ejecta model, the broadband light curves qualitatively resemble those of observed SNe Ia, peaking at a B-band magnitude around −19 about 20 days after explosion. Overall, the light curves calculated using our `Autostructure` derived linelist are rather similar to those calculated using the

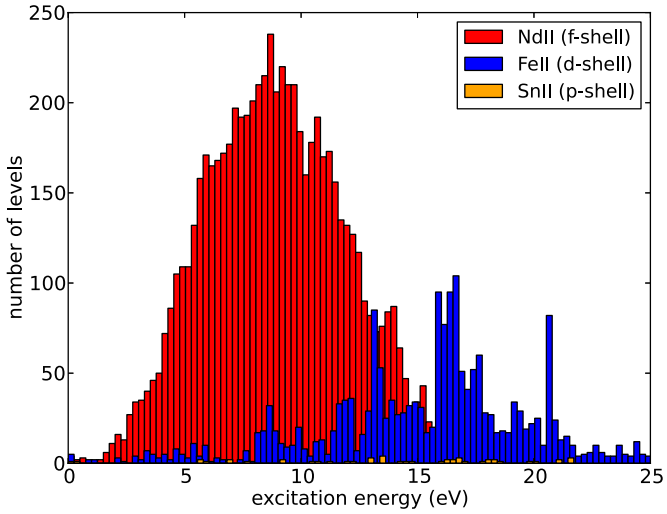

Figure 5. Histogram of the number of atomic levels vs. level energy (bin size = 0.25 eV) in our `Autostructure` models, which illustrates the much greater complexity of the lanthanide neodymium (with an open *f*-shell) as compared to iron (open *d*-shell) and tin (open *p*-shell).

(A color version of this figure is available in the online journal.)

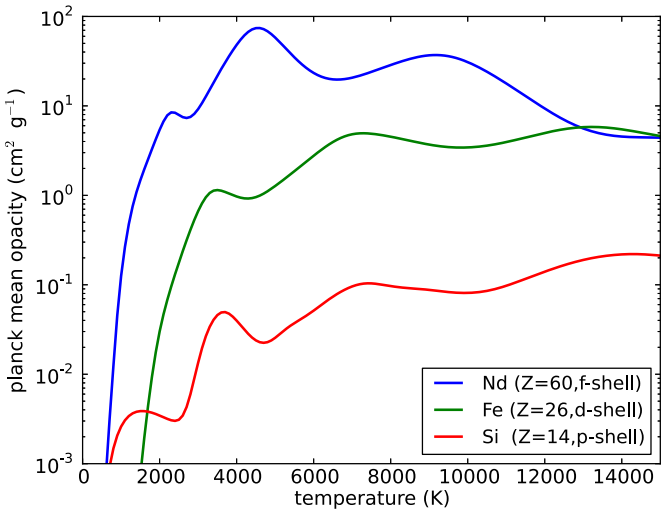

Figure 6. Planck mean expansion opacities for three different elements, showing the expected dependence on atomic complexity. The Nd opacities (blue line, $Z = 60$, open *f*-shell) were derived from `Autostructure` models, while the silicon (red line, $Z = 14$, open *p*-shell) and iron (green line, $Z = 26$, open *d*-shell) opacities used Kurucz line data. The calculations assume a density $\rho = 10^{-13}$ g cm^{-3} and a time since ejection $t_{\rm ej} = 1$ days.

(A color version of this figure is available in the online journal.)

Kurucz linelist, although differences up to 1 mag are seen at some epochs.

Figure 4 shows that the model spectrum (at 50 days after explosion) derived from the `Autostructure` linelist is also similar to that using Kurucz. Both calculations resemble the SED of an observed SN Ia. The `Autostructure` model does not reproduce the positions of most spectral features, which is to be expected given that the line wavelengths are only approximate. Even the Kurucz calculation fails to reproduce every observed spectral feature, as the underlying ejecta model did not include the IMEs present in real SNe Ia.

These results indicate that line data derived from our `Autostructure` models can be used to predict SN SEDs (but not line features) with some reliability. The general agreement of our synthetic observables with those of real SNe Ia suggests that—even with very crude knowledge of the underlying ejecta structure—we may still be able to predict the light curve and colors of radioactive transients to a reasonable level of accuracy.

5. HIGH Z OPACITIES

We have calculated structure models for several elements beyond the iron group, including tin (Sn, $Z = 50$, *p*-shell), cerium (Ce, $Z = 58$, *f*-shell), neodymium (Nd, $Z = 60$, *f*-block), and osmium (Os, $Z = 76$, *d*-shell). These species were chosen to sample different blocks on the periodic table corresponding to valence shells of different orbital angular momentum. The total number of atomic levels/lines determined by the structure models are listed in Table 1 and illustrated in Figure 5, and are generally consistent with the simple complexity estimates of Section 1.

As expected from simple physical arguments, we find that more complex atoms, in particular the lanthanides, have higher line expansion opacities. Figure 6 shows that the Planck mean opacity of neodymium is a factor ∼10–100 greater than that of iron, depending on the temperature. This is roughly consistent with the estimate one obtains by squaring the complexity measure (Equation (1)) to gauge the relative number of strong lines, $(C_{\rm Nd\,II}/C_{\rm Fe\,II})^2 \approx 22$.

The variation of the mean opacity with temperature (Figure 6) shows several bumps which reflect changes in the ionization state. As the temperature increases, the excited levels become more populated, and the number of optically thick lines increases. The opacity therefore increases with temperature until the gas becomes hot enough to ionize. This leads to multiple maxima in the mean opacity curve, each of which occur around the transition temperatures of the various stages of ionization. At sufficiently low temperatures, when the element becomes neutral, the opacities cut off sharply, and drop exponentially with decreasing temperature due to the Boltzmann factor in the excited state level populations.

An important property of the lanthanides is that, relative to the iron group, the opacity remains high at relatively low temperatures. This is because the ionization potentials of the lanthanides are generally ∼30% lower than those of the iron group (see Table 1). For neodymium, the mean opacity peaks at $T \approx 5000$ K, when the ion is mostly singly ionized and cuts offs at $T \lesssim 2500$ K when Nd becomes neutral. In comparison, the opacity peak for iron occurs at $T \approx 7000$ K and the neutral cutoff is at $T \lesssim 3500$ K. The general persistence of the lanthanide opacity to lower temperatures has an important impact on the color of the emergent spectra, contributing to cooler, redder photospheres.

Another important feature of the lanthanide opacity is the wavelength dependence—while the opacity decreases to the red (as there are more lines at bluer wavelengths), the decrease is much slower than that of the iron group (Figure 7). This is due to the much denser energy level spacing of the lanthanides, resulting in a much larger number of ∼1 eV optical/infrared transitions. The shallower opacity profile means that the lanthanides can line blanket not only UV wavelengths, but the entire optical region of the spectrum. This will influence the color of *r*-process SNe, as photons will eventually be reemitted or fluoresce (through the many lines) to infrared wavelengths where they may escape more easily.

As seen in Figure 7, the opacity of osmium ($Z = 76$) is very similar to that iron, despite the much higher atomic number. This is not surprising, as osmium is a homologue of iron, with a nearly half open *d*-shell. Similarly, the opacity of the lanthanide cerium

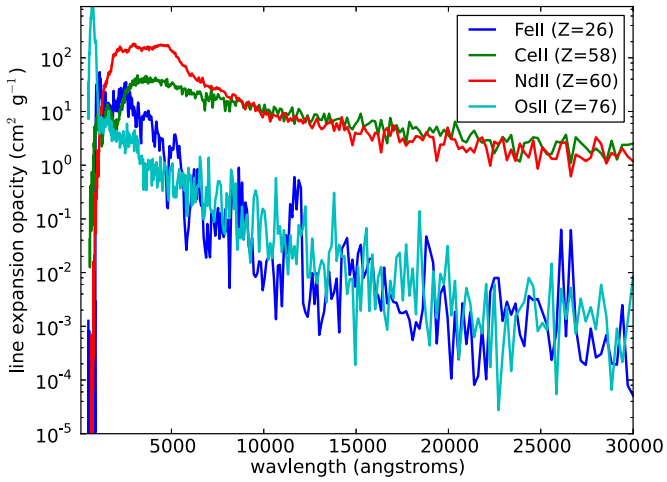

Figure 7. Wavelength-dependent line expansion opacities resulting from `Autostructure`-derived linelists. The opacity of the lanthanides (Nd, Ce) is much higher than iron and its *d*-shell homologue, osmium, especially in the infrared.

(A color version of this figure is available in the online journal.)

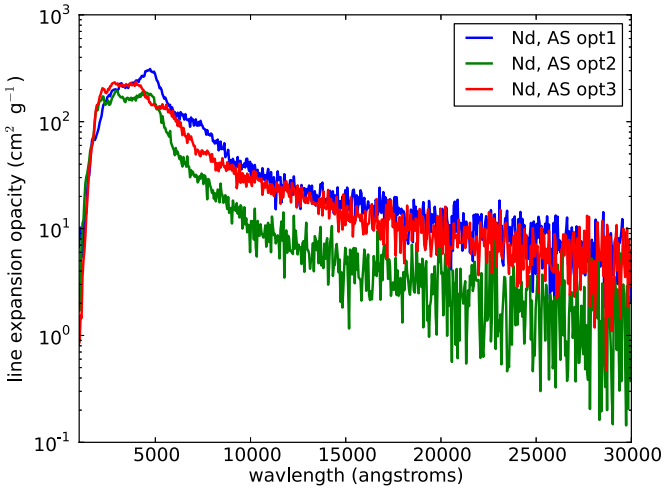

Figure 8. Variations in the wavelength-dependent expansion opacity for pure neodymium ($Z = 60$) ejecta obtained using different `Autostructure` optimization approaches. These calculations adopt a density $\rho = 10^{-13}$ g cm^{-3}, temperature $T = 4000$ K, time since ejection $t_{\rm ej} = 1$ days, and a wavelength binning $\Delta\lambda = 0.01\lambda$.

(A color version of this figure is available in the online journal.)

($Z = 58$) is comparable to, though slightly less than, that of neodymium. This confirms that species with similar complexity measures have roughly similar opacities, which we use to derive approximate opacities for *r*-process mixtures (Section 6).

5.1. Uncertainties and Comparison to Existing Data

Our derived opacities must possess some error, since the `Autostructure` model energies do not exactly match the experimental values (Figure 2). To estimate how sensitive the results are to the detailed level energy structure and configuration ordering, we examined the Nd II opacities derived from the three different optimization schemes described in Section 3. The resulting variation provides an estimate of our level of uncertainty.

Figure 8 shows that the opacities calculated using the *opt1* and *opt3* models are quite similar, while the *opt2* model opacities are lower by a factor of ∼5 at some wavelengths. The *opt2* model has relatively higher energy levels, and hence smaller excited state LTE level populations, which is presumably the reason for the lower opacities. The *opt1* and *opt3* models had similar level energies, but the ground state configuration and ordering were different. These results suggest that what matters most to the opacities is the energy level spacing, and not the exact configuration ordering. Given that the low lying *opt3* Nd II level energies reproduce the experiment fairly well, we suspect that further fine tuning of the `Autostructure` model is unlikely to change the resulting opacity by much more than a factor of ∼2.

We have also compared our `Autostructure` opacities to existing line data from the VALD database, which collects atomic data from a variety of sources (Heiter et al. 2008). The only high-Z ions with enough lines in VALD to derive expansion opacities are Ce II and Ce III, which have wavelengths and oscillator strengths calculated by the Mons group (Biémont et al. 1999; Palmeri et al. 2000; Quinet & Biémont 2004). The approach taken by the Mons group to determine atomic structure is the same as that of Kurucz, viz., calculations with Cowan's code utilizing extensive experimental energies. In Figure 9, we compare the expansion opacities of Ce calculated using the VALD linelist and our own `Autostructure` list. The agreement in both the mean- and wavelength-dependent values is good to a factor of ∼2. Our conclusions about the size and wavelength dependence of the lanthanide opacities are therefore confirmed when using radiative data from independent structure calculations.

6. OPACITIES OF *r*-PROCESS MIXTURES

Although we have only calculated atomic structure models for a few ions, the results (Figure 7) suggest that ions of similar complexity have roughly similar opacities. This allows us to construct approximate *r*-process mixtures based on the representative cases.

In an *r*-process mixture, the abundance of any individual lanthanide is relatively low ($\lesssim$1%). Nevertheless, these species likely dominate the total opacity. In fact, the opacity will depend rather weakly on the exact lanthanide abundance. This is because for the conditions found in NSM ejecta, many of the strong lanthanides lines are extremely optically thick ($\tau_s \gg 1$). Such lines contribute equally to the expansion opacity regardless of the ion's abundance, just as long as that abundance remains high enough to keep τ_s above unity.

We illustrate this weak dependence on lanthanide abundance in Figure 10, by computing the opacity of a mixture of neodymium and iron. Decreasing the Nd mass fraction by a factor of 10 (from 100% to 10%) only reduces the total opacity of the mixture by ∼40%. Decreasing the Nd mass fraction by two orders of magnitudes (from 100% to 1%) reduces the total opacity of the mixture by a factor of five. We find that the Nd opacity dominates over that of iron as long as its mass fraction is $\gtrsim 10^{-4}$.

The actual *r*-process ejecta from NSMs will be a heterogeneous mixture of many high Z elements. This multiplicity of species should enhance the opacity, as each ion contributes a distinct series of lines. To estimate the opacity of the mixture, we assume the line data of Nd is representative of all *f*-shell species (the lanthanides) and that iron is representative of all *d*-shell elements. We ignore the *s*-shell and *p*-shell elements since their opacities will be very low. We then construct the expansion opacity of the mixture by generalizing Equation (9)

$$\kappa_{\rm mix}(\lambda) = \sum_Z \frac{\xi_Z}{\rho c t_{\rm ej}} \sum_i \frac{\lambda_i}{\Delta\lambda_i}(1 - \exp[-\tau_i(\rho_Z)]) \qquad (15)$$

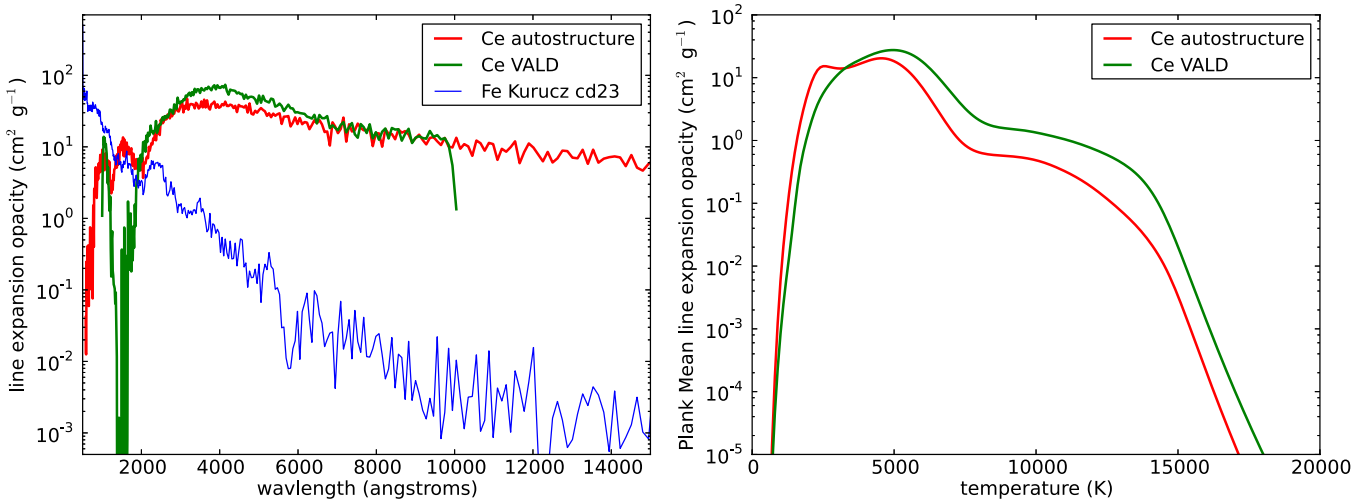

Figure 9. Comparison of the expansion opacity for pure cerium ($Z = 58$) ejecta, computed using the `Autostructure` line data (red lines) and the VALD linelist (green lines). The calculations assume a density $\rho = 10^{-13}$ g cm^{-3}, time since ejection $t_{\rm ej} = 1$ days, and a wavelength binning $\Delta\lambda = 0.01\lambda$. Left: line expansion opacity vs. wavelength for a temperature $T = 5000$ K. At optical wavelengths, the `Autostructure` results are in reasonably good agreement with the VALD; both are orders of magnitude higher than the opacity of pure iron ejecta (brown line). Right: Planck mean opacity as a function of temperature. Only Ce II and Ce III are included in the calculation.

(A color version of this figure is available in the online journal.)

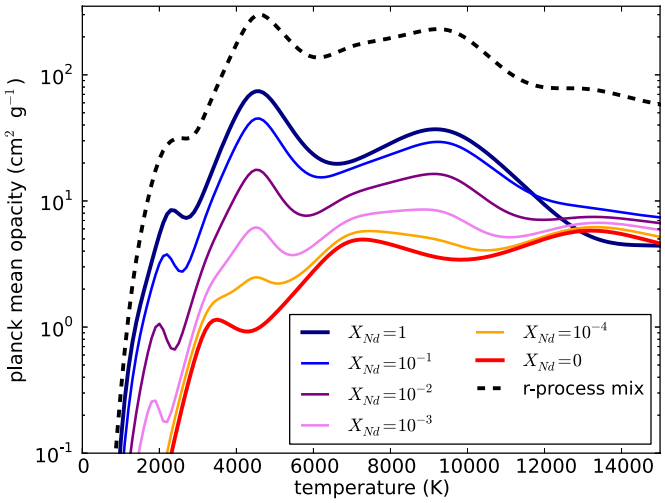

Figure 10. Dependence of the mean expansion opacity on the abundance of lanthanides. The solid lines show the Planck mean opacity for various mass fractions of neodymium in a mixture with iron. The dashed line shows the opacity of the approximate *r*-process mixture (with all 14 lanthanides) discussed in Section 6.

(A color version of this figure is available in the online journal.)

where the sum Z runs over the representative ions (in this case only Fe and Nd) and the quantity ξ_Z specifies the total number of elements represented by each. For Nd, $\xi_Z = 14$ to account for all 14 lanthanides, while for iron $\xi_Z = 30$ to account for all *d*-shell elements between $21 \leqslant Z \leqslant 80$. The quantity $\rho_Z = X_Z \rho$ is the density of the representative elements, where X_Z is the mass fraction of each. As an illustrative *r*-process mixture, we assume that the average mass fraction of each lanthanide is $X_f = 1\%$, and the average *d*-shell species fraction is $X_d = 2\%$. The remainder of the composition was taken to be calcium (*s*-shell) as a neutral filler. We used the Nd line data from the *opt3* structure model, and the iron line data from the Kurucz CD23 list.

The dashed line in Figure 10 shows the Planck mean opacity of our approximated *r*-process mixture. Because each of the 14 lanthanides is assumed to contribute independently in the sum, the total opacity is essentially 14 times that of the mixture with only 1% Nd. At certain temperatures when the lanthanide opacity dips, the *d*-shell opacity makes a comparable contribution. We note that opacity of the mixture can approach the saturation level discussed in Section 2.4, such that our assumption that the strong lines do not overlap can be called into question.

7. SPECTRA OF NS MERGER EJECTA

To illustrate the general effect of our *r*-process opacities on the emission from NSM ejecta, we have calculated model spectra using the `Sedona` radiation transport code (Kasen et al. 2006). A more comprehensive discussion of the light curves and colors of these transients, and their dependence on the ejecta parameters, is given in Barnes & Kasen (2013).

As a simple, fiducial ejecta model, we considered a spherically symmetric, homologously expanding remnant with a broken power-law density profile. The total ejecta mass was taken to be $M_{\rm ej} = 0.01\ M_\odot$ and the kinetic energy $E = 1/2 M_{\rm ej} v_c^2$ with a characteristic velocity $v_c = 0.1c$. The transport calculations assume that the ionization/excitation state is given by LTE, and that the line source function is described by the Planck function, i.e., the medium is purely absorbing. In reality, the probability of absorption in lines may be small, with fluorescence being the more likely result of line interactions. However, SN transport calculations have shown that for complex ions, repeated fluorescence among a multitude of lines has an approximately thermal character (Pinto & Eastman 2000; Kasen 2006). We use the opacities of an *r*-process mixture derived in Section 6.

The high opacity of *r*-process material has a significant impact on the predicted radioactive transients from NSMs (Figure 11). Compared to previous calculations (which assumed iron-like opacities), the predicted bolometric light curve is of much longer duration, $\sim$1 week as opposed to $\sim$1 day. This is due to the longer effective diffusion time through the more opaque ejecta. The peak luminosity is also lower, as the radiation suffers greater loses due to expansion over this period.

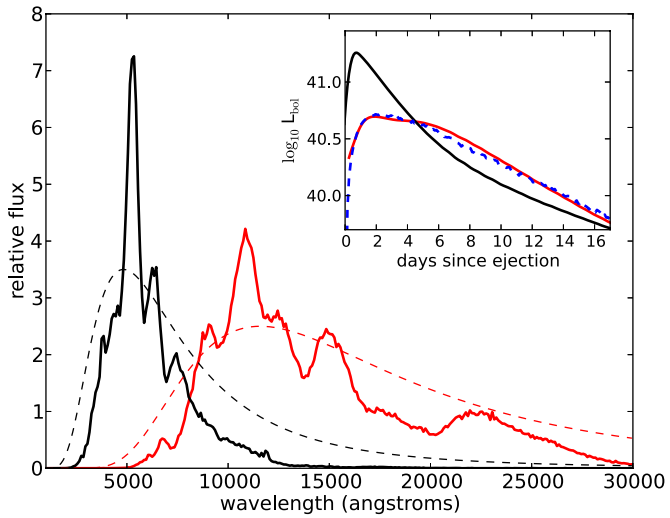

Figure 11. Synthetic spectra (2.5 days after mass ejection) of the *r*-process SN model described in the text, calculated using either Kurucz iron group opacities (black line) or our `Autostructure`-derived *r*-process opacities (red line). For comparison, we overplot blackbody curves of temperature $T = 6000$ K (black dashed) and $T = 2500$ K (red dashed). The inset shows the corresponding bolometric light curves assuming iron (black) or *r*-process (red) opacities. For comparison, we also plot a light curve calculated with a gray opacity of $\kappa = 10$ cm^2 g^{-1} (blue dashed line).

(A color version of this figure is available in the online journal.)

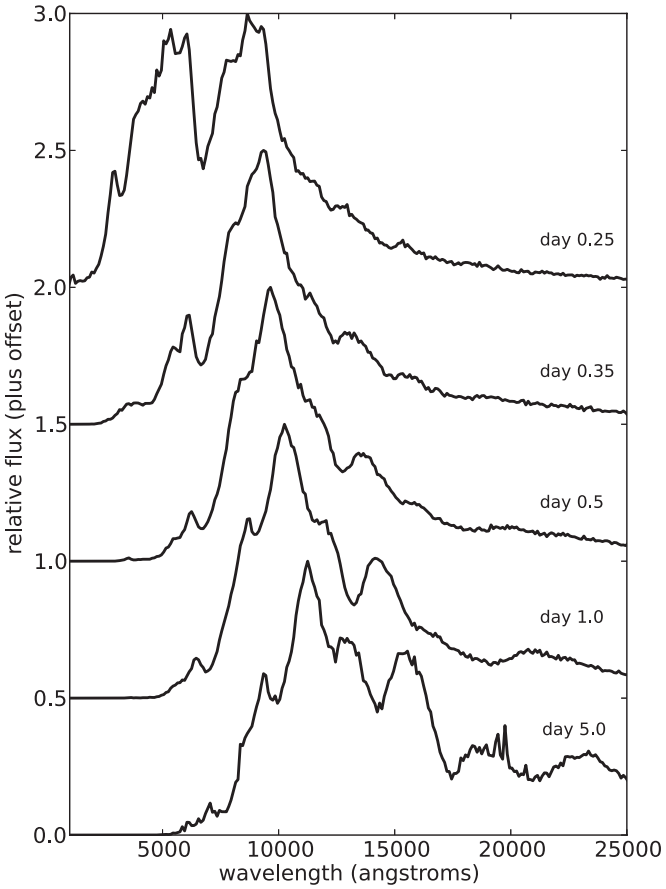

Figure 12. Synthetic spectra time series of the *r*-process SN model described in the text. The times since mass ejection are marked on the figure.

The spectrum at 2.5 days after the merger is much redder, with most of the flux emitted in the near infrared ($\sim$1 μm). Due to the extreme line blanketing at bluer wavelengths, the photons are eventually redistributed (through lines) to the infrared, where the opacities are lower and radiation can escape more readily. As shown in Figure 11, the bolometric light curve from the full multi-wavelength calculation resembles one calculated with an effective gray opacity of $\kappa = 10$ cm^2 g^{-1}, which is two orders of magnitude greater than values used in previous gray transport models.

Other than the unusually red color, the *r*-process spectra generally resemble those of ordinary SNe, and in particular those with high expansion velocities (e.g., the hyper-energetic Type Ic event, SN 1998bw; Galama et al. 1998). The continuum flux, which is produced by emission in the Doppler-broadened forest of lines, resembles a blackbody with a few broad ($\sim$200 Å) spectral features. It is not easy to associate these features with either absorption or emission from a single line; instead they arise from blends of many lines. Because our atomic structure models do not accurately predict line wavelengths (and we only include lines of Nd and Fe), the location of the features in our synthetic spectra are not to be trusted. Nevertheless, the model spectra are likely qualitatively correct. One can anticipate where features are most likely to appear by examining the energy spacing of the low lying levels of the lanthanides.

Figure 12 shows the time evolution of the synthetic spectra. At the earliest times ($\lesssim$0.25 days after ejection) some flux emerges at optical wavelengths, but this phase is short lived. By day 0.5, the optical emission has faded, and the spectra evolve relatively slowly thereafter, with effective blackbody temperatures steady in the range $T \approx$ 2000–3000 K. The temporal evolution can be understood by considering the mean opacity curves (e.g., Figure 6). At early times, the ejecta is relatively hot ($\gtrsim$4000 K) throughout, and the opacity is roughly constant with radius. By day $\sim$0.3, however, the outermost layers have cooled below $\lesssim$3000 K, and the *r*-process opacities drop sharply due to lanthanide recombination. The ejecta photosphere forms near the recombination front (as overlying neutral layers are essentially transparent) which regulates the effective temperature to be near the recombination temperature. This behavior is similar to the plateau phase of the (hydrogen-rich) Type IIP SNe, although in this case the opacity is due to line blanketing, not electron-scattering. More importantly, the temperature at the recombination front ($T_I \sim 2500$ K) is a factor of $\sim$2 lower for *r*-process ejecta, as the ionization potentials of the lanthanides ($\sim$6 eV) are lower than that of hydrogen ($\sim$13.6 eV).

Our calculated SEDs are somewhat sensitive to the atomic structure model used to generate the line data. Figure 13 compares calculations using line data from the different `Autostructure` optimization runs (*opt1, opt2,* and *opt3*). The observed differences can be taken as some measure of the uncertainty resulting from inaccuracies in our atomic structure calculations. Notably, the spectrum calculated using the *opt2* linelist has significantly higher flux in the optical ($\sim$6000 Å). This is presumably due to the lower overall opacity of the *opt 2* model (Figure 8). Given the superior match of the *opt3* model to the experimental level data, we consider the spectral predictions using this line data to be the most realistic; however, it is clear that some significant uncertainties remain.

Another concern for the spectrum predictions is the potential breakdown of the Sobolev approximation. At bluer wavelengths, the mean spacing of strong lines can become less than the intrinsic (presumed thermal) width of the lines, which violates the assumptions used to derive an expansion opacity. It is not

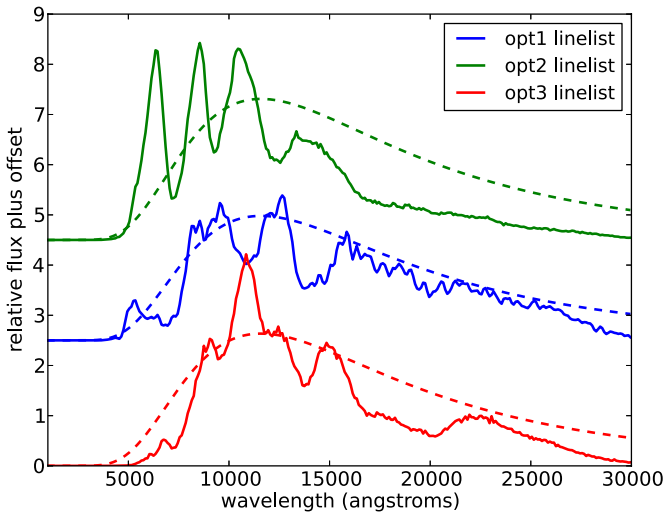

Figure 13. Effect of varying the atomic structure model on the predicted observables of an *r*-process SN. The figure shows the synthetic spectrum (2.5 days after ejection) calculated using `Autostructure` linelists under different optimization schemes. The dashed lines show, for comparison, blackbody curves of temperature $T = 2500$ K.

(A color version of this figure is available in the online journal.)

immediately clear how this will impact the results. Two lines that overlap exactly will behave like a single line, which suggests that an overlapping line should be discounted, not double counted. In this case, the opacity should saturate at a maximum value $\kappa_{\rm sat}$ (Equation (11)). On the other hand, in this saturation limit, photons can no longer escape lines by redshifting past them, as there are no longer any optically thin "windows" between lines. The individual line optical depths then become relevant, and the effective opacity may be larger than one would estimate from the expansion formalism. In practice, the impact of line overlap may not be so dramatic—the opacity generically declines to longer wavelength, and the net effect of the transport is to distribute photons to the red/infrared where saturation may no longer be an issue. To address the question in detail will require radiative transport calculations that dispense with the Sobolev approximation and resolve individual line profiles.

8. SUMMARY AND CONCLUSIONS

The opacity of *r*-process ejecta is orders of magnitude higher than that of ordinary SN debris, a fact we have demonstrated using new atomic structure calculations (Figure 7), preexisting line data (Figure 9), and simple physical counting arguments (Figure 1). There are two physical reasons for the high opacity: (1) *Complexity:* the *r*-process composition includes rare elements with complex valence electron structure, in particular the lanthanides which have an open valence $4f$-shell. Such elements have a significantly greater number of levels and lines, which results in an overall higher expansion opacity; (2) *Multiplicity:* the *r*-process produces a heterogenous mixture of many elements, each of which contributes a distinct series of lines. Since the expansion opacity depends on the total number of strong lines (and not the strength of any individual line) this diversity of the mixture enhances the opacity relative to a more homogenous composition. Although the *r*-process opacities have a complicated wavelength and temperature dependence, in simple transport models using a gray opacity of $\kappa = 10$ cm^2 g^{-1} is found to be a fairly effective for calculating the bolometric light curves from NSM outflows.

While our *r*-process opacity calculations offer a significant improvement over previous estimates (which were little more than educated guesses), several uncertainties remain. The `Autostructure` models only approximate the level structure of the high-Z elements, and so do not correctly predict the wavelength of individual transitions. Fortunately, the pseudo-continuum opacities depend only on the statistical distribution of lines and are fairly robust, although our numerical experiments indicate uncertainties at the factor of $\sim$2 level. In the future, we can iteratively tune the structure models to better reproduce the observed energy levels, although this is a time-consuming process. Moreover, many of the high-Z ions lack good experimental level data.

Another more important uncertainty is that we have used the radiative data for one species (Nd, $Z = 60$) to represent all lanthanides. In fact, not all lanthanides are equal—the ions whose valence *f*-shell is nearly open (e.g., La, $Z = 56$) or closed (Yb, $Z = 70$) are considerably less complex, and should have correspondingly lower opacities. On the other hand, gadolinium (Gd, $Z = 64$) has a nearly half-filled *f*-shell, and is one of the most complex species on the periodic table. Simple counting arguments (Figure 1) suggest that Gd may have an opacity $\gtrsim$10 times that of Nd. We therefore suspect that our current opacities *underestimate* the true values for an *r*-process mixture where Gd is present at the $\sim$1% level. In future work, we will quantify the line data for all lanthanides. The actinides should also be considered, as they are open *f*-shell as well, although only a few species (e.g., uranium) likely have high enough abundance to make a difference. In total, the atomic data required for *r*-process opacities is massive, involving numerous structure calculations and many billions of lines.

The high opacity of *r*-process material has significant implications for discovering and interpreting the radioactively powered transients associated with NSMs. With more realistic opacities, the predicted light curves are of longer duration and dimmer at peak (see Barnes & Kasen 2013). Perhaps even more important to detection is that the SED is shifted into the infrared, peaking at $\sim$1 μm. This is due to the strong line blanketing at optical wavelengths, which pushes the photosphere out to cooler layers ($T \sim 2500$ K) where the lanthanides recombine and become more transparent. Other than the very red color, the spectra qualitatively resemble those of other high-velocity SNe, with a pseudo blackbody continuum and broad ($\sim$200 Å) spectral features.

The predicted emission at optical wavelengths is somewhat sensitive to the details of the opacity and its associated uncertainties. Spectra calculated using our *opt2* radiative data were fairly bright in the *V*-band ($\sim$5000 Å), while those calculated using *opt3* data had almost no flux at these wavelengths. Because the level structure of our *opt3* model agrees better with experiment (and given that the overall opacity may be even higher than our Nd-based estimates) we consider the latter case to be the more likely reality. However, the opacities are still not fully converged, and we cannot altogether rule out the possibility that *r*-process SNe may emit some persistent emission in the optical.

These results suggest that (to the extent possible) it is worthwhile to search for and/or follow up gravitational wave sources at red or infrared wavelengths. Optical surveys, however, may still have a chance to discover a radioactive transient if it is caught very early ($\lesssim$1 day) or if some of the ejecta is nearly lanthanide-free. In fact, it is likely that, in addition to the tidal tails, a second component of lighter elements ($Z \lesssim 50$) is ejected from a post-merger disk wind. If this wind includes

radioisotopes with appropriate half-lives (e.g., ^{56}Ni), the light curve may be relatively bright and peak in the optical. A detailed understanding of the wind nucleosynthesis and mixing with the tails is important, as our results suggest that contamination by lanthanides at just the 10^{-3} level may significantly raise the opacities.

Beyond detection, a significant observational challenge will be confirmation that a transient is indeed due to a NSM. There are likely many classes of stellar explosions that produce low mass ejections of radioactive material (e.g., Bildsten et al. 2007; Moriya et al. 2010), and an increasing number of fast, faint transients have been observed at optical wavelengths (e.g., Kasliwal et al. 2010, 2012; Perets et al. 2010; Foley et al. 2013). Fortunately, our calculations demonstrate that the optical properties of *r*-process ejecta differ dramatically from transients due to lower mass isotopes. A key distinguishing feature is that the *r*-process SED peaks in the infrared with a nearly constant color temperature regulated to the lanthanide recombination temperature, ∼2500 K. The population of brief, infrared variables is mostly unknown, but it is possible that the infrared transient sky is much cleaner than the optical one.

By comparing observations of an *r*-process SN to light curve models, one could presumably constrain the mass of heavy nuclei ejected in an compact object merger, which would go a long way to understanding the unknown site(s) of the *r*-process. One would like to go further and spectroscopically study the abundance distribution of the outflows. That will be challenging—the lines are heavily blended and we do not have accurate wavelengths for all of them. In the future, however, we can refine the line data by tuning structure models to match experimental data (where available) and use radiative transport calculations to quantify how global abundances variations affect the blended features. While measuring a detailed abundance pattern will be difficult, spectroscopic modeling may someday allow strong constraints on the amount and gross composition of ejecta.

This assumes that radioactive *r*-process transients exist and that we can find them. Admittedly, we test dangerous waters any time that, lacking observational input, we attempt to describe a new astrophysical phenomenon on purely theoretical grounds. The situation here is a step more treacherous; not only must we rely on simulations of a complex macroscopic system, even the *microscopic* structures of our ions are model-based. Obviously, observational input is needed to ground the theory. In the meantime, the numerical experiment presented in Section 4.2 may offer a bit of comfort. In that example, we calculated the light curve of an obliviously crude model of a SN Ia (a uniform ^{56}Ni blob) using opacities derived entirely from ab initio atomic structure models. Despite deliberately ignoring decades of work in the field, our "SN from scratch" predictions were not all that bad, and certainly good enough to allow one to search for and identify a thermonuclear event. There is then reason to hope that the predictions for *r*-process SNe are (or will soon be) good enough for us to know one when we see one.

This work was supported by the Department of Energy Office of Nuclear Physics Early Career Award, and by the Director, Office of Energy Research, Office of High Energy and Nuclear Physics, Divisions of Nuclear Physics, of the U.S. Department of Energy under Contract No. DE-AC02-05CH11231. The work of N.R.B. was supported by STFC (ST/J000892/1).

REFERENCES

Arnett, W. D. 1980, ApJ, 237, 541
Arnett, W. D. 1982, ApJ, 253, 785
Arnould, M., Goriely, S., & Takahashi, K. 2007, PhR, 450, 97
Badnell, N. R. 2011, CoPhC, 182, 1528
Badnell, N. R., Ballance, C. P., Griffin, D. C., & O'Mullane, M. 2012, PhRvA, 85, 052716
Badnell, N. R., Bautista, M. A., Butler, K., et al. 2005, MNRAS, 360, 458
Barnes, J., & Kasen, D. 2013, ApJ, in press
Biémont, E., Palmeri, P., & Quinet, P. 1999, Ap&SS, 269, 635
Bildsten, L., Shen, K. J., Weinberg, N. N., & Nelemans, G. 2007, ApJL, 662, L95
Chawla, S., Anderson, M., Besselman, M., et al. 2010, PhRvL, 105, 111101
Cowan, R. D. 1981, Theory of Atomic Structure and Spectra (Berkeley, CA: Univ. California Press)
Cowan, R. D., & Griffin, D.C. 1976, JOSA, 66, 1010
Eastman, R. G., & Pinto, P. A. 1993, ApJ, 412, 731
Eichler, D., Livio, M., Piran, T., & Schramm, D. N. 1989, Natur, 340, 126
Foley, R. J., Challis, P. J., Chornock, R., et al. 2013, ApJ, 767, 57
Freiburghaus, C., Rosswog, S., & Thielemann, F.-K. 1999, ApJL, 525, L121
Galama, T. J., Vreeswijk, P. M., van Paradijs, J., et al. 1998, Natur, 395, 670
Goriely, S., Bauswein, A., & Janka, H.-T. 2011, ApJL, 738, L32
Heiter, U., Barklem, P., Fossati, L., et al. 2008, JPhCS, 130, 012011
Hotokezaka, K., Kiuchi, K., Kyutoku, K., et al. 2013, PhRvD, 87, 024001
Janka, H.-T., Eberl, T., Ruffert, M., & Fryer, C. L. 1999, ApJL, 527, L39
Karp, A. H., Lasher, G., Chan, K. L., & Salpeter, E. E. 1977, ApJ, 214, 161
Kasen, D. 2006, ApJ, 649, 939
Kasen, D., Röpke, F. K., & Woosley, S. E. 2009, Natur, 460, 869
Kasen, D., Thomas, R. C., & Nugent, P. 2006, ApJ, 651, 366
Kasliwal, M. M., Kulkarni, S. R., Gal-Yam, A., et al. 2010, ApJL, 723, L98
Kasliwal, M. M., Kulkarni, S. R., Gal-Yam, A., et al. 2012, ApJ, 755, 161
Kelley, L. Z., Mandel, I., & Ramirez-Ruiz, E. 2013, PhRvD, 87, 123004
Kochanek, C. S., & Piran, T. 1993, ApJL, 417, L17
Kramida, A., Ralchenko, Yu., Reader, J., & NIST ASD Team. 2012, NIST Atomic Spectra Database (Gaithersburg, MD: NIST), http://physics.nist.gov/asd
Kulkarni, S. R. 2005, arXiv:astro-ph/0510256
Kurucz, R. 1993, Atomic Data for Opacity Calculations. Kurucz CD-ROM No. 1 (Cambridge, MA: Smithsonian Astrophysical Observatory), 1
Kurucz, R., & Bell, B. 1995a, in Atomic Line Data, Kurucz CD-ROM No. 23 (Cambridge, MA: Smithsonian Astrophysical Observatory), 23
Kurucz, R. L., & Bell, B. 1995b, Kurucz CD-RoM (Cambridge, MA: Smithsonian Astrophysical Observatory)
Lattimer, J. M., & Schramm, D. N. 1974, ApJL, 192, L145
Lee, W. H. 2001, MNRAS, 328, 583
Levinson, A. 2006, ApJ, 648, 510
Li, L.-X., & Paczyński, B. 1998, ApJL, 507, L59
Mandel, I., & O'Shaughnessy, R. 2010, CQGra, 27, 114007
Metzger, B. D., & Berger, E. 2012, ApJ, 746, 48
Metzger, B. D., Martínez-Pinedo, G., Darbha, S., et al. 2010, MNRAS, 406, 2650
Metzger, B. D., Piro, A. L., & Quataert, E. 2008, MNRAS, 390, 781
Metzger, B. D., Piro, A. L., & Quataert, E. 2009, MNRAS, 396, 304
Moriya, T., Tominaga, N., Tanaka, M., et al. 2010, ApJ, 719, 1445
Nissanke, S., Kasliwal, M., & Georgieva, A. 2013, ApJ, 767, 124
Oechslin, R., Janka, H.-T., & Marek, A. 2007, A&A, 467, 395
Palmeri, P., Quinet, P., Wyart, J.-F., & Biémont, E. 2000, PhyS, 61, 323
Perets, H. B., Gal-Yam, A., Mazzali, P. A., et al. 2010, Natur, 465, 322
Phinney, E. S. 2009, in Astro2010: The Astronomy and Astrophysics Decadal Survey, 235
Pinto, P. A., & Eastman, R. G. 2000, ApJ, 530, 757
Piran, T., Nakar, E., & Rosswog, S. 2013, MNRAS, 730, 2121
Quinet, P., & Biémont, E. 2004, ADNDT, 87, 635
Roberts, L. F., Kasen, D., Lee, W. H., & Ramirez-Ruiz, E. 2011, ApJL, 736, L21
Rosswog, S. 2005, ApJ, 634, 1202
Rosswog, S., Liebendörfer, M., Thielemann, F.-K., et al. 1999, A&A, 341, 499
Rybicki, G. B., & Lightman, A. P. 1986, Radiative Processes in Astrophysics (New York: Wiley)
Schutz, B. F. 1986, Natur, 323, 310
Shibata, M., & Taniguchi, K. 2011, LRR, 14, 6
Sim, S. A., Röpke, F. K., Hillebrandt, W., et al. 2010, ApJL, 714, L52
Sneden, C., Cowan, J. J., & Gallino, R. 2008, ARA&A, 46, 241
Sobolev, V. V. 1960,
Surman, R., McLaughlin, G. C., & Hix, W. R. 2006, ApJ, 643, 1057
Surman, R., McLaughlin, G. C., Ruffert, M., Janka, H.-T., & Hix, W. R. 2008, ApJL, 679, L117
Sylvestre, J. 2003, ApJ, 591, 1152